Available online at www.sciencedirect.com
ScienceDirect
Journal of Catalysis 251 (2007) 459–473
JOURNAL OF CATALYSIS
www.elsevier.com/locate/jcat

Vanadia-based SCR catalysts supported on tungstated and sulfated zirconia: Influence of doping with potassium

Johannes Due-Hansen [a,*], Soghomon Boghosian [b], Arkady Kustov [a], Peter Fristrup [a], George Tsilomelekis [b], Kenny Ståhl [a], Claus Hviid Christensen [a], Rasmus Fehrmann [a,*]

[a] *Department of Chemistry and Center for Sustainable and Green Chemistry, Technical University of Denmark, 2800 Lyngby, Denmark*
[b] *Department of Chemical Engineering, University of Patras and FORTH/ICE-HT, GR-26500 Patras, Greece*

Received 19 April 2007; revised 13 July 2007; accepted 13 July 2007

Available online 5 September 2007

Abstract

A series of vanadium-based SCR catalysts supported on sulfated or tungstated ZrO_2 were synthesized and characterized by means of N_2-BET, XRD, NH_3-TPD and in situ Raman spectroscopy. The effect of potassium doping on the properties of vanadia species was studied in detail. A number of catalyst preparation parameters were examined, including the choice of precipitant, variation of carrier surface area, potassium poisoning, crystallinity, and ZrO_2-phase composition. The results show that the catalyst structure and SCR activity are affected from the synthesis route by the support crystallinity and morphology, the surface composition, and the molecular configuration of the dispersed vanadates. It was observed that poisoning with potassium had a negligible effect on the surface vanadate species (especially the V=O stretching frequency observed by in situ Raman spectroscopy) if supported on the sulfated zirconia. Conversely, a more pronounced influence on the structure of surface vanadate was observed for the corresponding unsulfated samples, in which a significant red shift in the V=O stretching frequency was observed on potassium doping. Computational studies suggested that potassium was responsible for both the observed decrease in V=O stretching frequency and the higher proportion of dimers and higher polymers through coordination between K^+ and two neighbouring V=O. The results suggest an increased resistance toward potassium doping for the vanadia-based catalysts supported on sulfated zirconia.

Keywords: NO SCR with ammonia; Potassium poisoning; Biomass; Deactivation; Tungstated zirconia; Sulfated zirconia; Vanadium oxide; In situ Raman spectroscopy; DFT calculations

1. Introduction

The selective catalytic reduction (SCR) of NO_x by NH_3 in the presence of O_2 remains among the state-of-the-art technologies for controlling NO_x emissions from stationary sources, even though alternative strategies are under intensive development. Transition metal oxides (most commonly vanadia) supported on anatase and promoted with tungsten or molybdenum oxides are the most active SCR catalysts used on an industrial scale at 300–450 °C. Numerous studies have been published related to catalytic activity, reaction mechanism, effects of vanadia loading, effects of active phase composition, and other pertinent topics; these have been summarized in several recent reviews [1,2]. Concerning the reaction mechanism, most research findings suggest the dual-site Eley–Rideal mechanism involving a surface vanadia redox site and an adjacent nonreducible acid–base site [3–5]. The key and rate-determining step in this mechanism is assumed to be the activated adsorption of ammonia on the V^{5+}–OH Brøndsted acid site, which reduces a nearby V^{5+}=O redox site to V^{4+}. This activated intermediate V^{4+}–OH, is very reactive toward gaseous NO, leading to the products, N_2 and H_2O, which desorb from the surface [3–7].

The use of biomass as an alternative to fossil fuels has attracted increased interest because it is considered CO_2-neutral with regard to the human impact on the CO_2 content in the atmosphere. However, a major disadvantage of using biomass is the resulting fast deactivation of the SCR catalyst. Commercial

* Corresponding authors.
E-mail addresses: jdh@kemi.dtu.dk (J. Due-Hansen), rf@kemi.dtu.dk (R. Fehrmann).

0021-9517/$ – see front matter
doi:10.1016/j.jcat.2007.07.016

SCR catalysts, consisting of TiO_2 as a high-surface area support and V_2O_5–WO_3 as the active component, deactivates about three to four times faster than what is observed in conventional coal-fired installations. The main reason for this deactivation is the presence of high amounts of potassium (up to 2 wt% in straw), which acts as a poison for the catalyst [8]. Therefore, there is a need for new SCR catalysts that are more resistant to deactivation by alkali metals, especially potassium. There exist only few studies dealing with the effect of alkali oxide additives on the activity and physicochemical properties of the vanadium-based catalysts. The influence of alkali metals on the activity of V_2O_5/TiO_2 catalysts has been reported by several authors [9–12], most of whom concluded that poisonous additives are affecting the Brønsted acid sites, which are responsible for ammonia adsorption, thus decreasing both their number and activity in NO reduction. Different strategies are available to regenerate deactivated catalysts; for example, washing with a solution of diluted sulfuric acid enables complete restoration of the initial activity of the catalyst [8,13]. The major disadvantage of such procedures is that in most cases, the power plant must be closed down to regenerate the deactivated catalyst. Another efficient way to overcome the deactivation problems could be to use an alternative catalyst with greater resistance toward poisoning with potassium. In this context, the use of highly acidic sulfated or tungstated zirconia as a support for vanadia-based SCR catalysts has been reported to enhance catalyst resistance toward alkali poisoning to some extent [14,15], although these early studies performed no comprehensive characterization of the surface and the influence of potassium on the vanadium species.

The surface composition under operating conditions is a subject of discussion, and the molecular structure and configurations of the catalytically active components are under debate. In this respect, the reported influence of specific oxide supports, along with the observed stability of terminal V=O bonds during the SCR reaction [5], suggests that the V–O–support bond is involved in the rate-determining step. It has been shown that the SCR activity of a series of transition metal oxides supported on TiO_2 correlates well with the extent of interactions between the active phase and the support [16]. Finally, structure–activity relationships based on in situ FTIR and Raman spectra, in combination with data from catalytic experiments, suggest that the active sites are most probably pairs of surface vanadate species in close proximity to each other [4,17]. Thus, it seems that the combination of an electronic effect of the support on the V=O redox site and the presence of adjacent Brønsted sites are needed for the creation of a highly active catalysts. Anatase is known to fulfill this requirement, whereas silica is not.

The present work, in contrast to our previous work on this subject [14,15], is concerned with the synthesis and multidisciplinary characterization of vanadium-based SCR catalysts supported on sulfate- or tungstate-promoted ZrO_2, particularly the effect of potassium doping on the properties of vanadia species and catalytic activity. In addition, it examines the influence of various catalyst preparation parameters, including the choice of precipitant, variation of carrier surface area, potassium poisoning, crystallinity, and ZrO_2-phase composition. To gain insight into the structure and deactivation of the catalytically active species by potassium, density functional calculations were applied and possible surface configurations investigated.

2. Experimental

2.1. Catalyst preparation

The zirconium oxide was prepared using two procedures adapted from previous work [18,19]: a one-step synthesis, in which tungsten oxide and hydrous zirconia are coprecipitated, and a two-step method, in which the precipitated hydrous zirconia is subsequently immersed into a diluted solution of sulfuric acid. The resulting tungstated or sulfated hydrous zirconia was then dried and calcined at 700 °C. The overall synthesis route is summarized in Scheme 1.

Zirconyl nitrate hydrate, ($ZrO(NO_3)_2{\cdot}nH_2O$, 27% Zr, Fluka), was dissolved in water at room temperature with ammonium metatungstate (Purum >97%) to obtain 20 wt% WO_3/ZrO_2 after calcination. This WO_3 content was selected based on the studies of Sohn et al. [20] and Santiesteban et al. [18], who found the maximum surface acidity at 20 wt% loading of WO_3 on zirconia. In previous work [15], the calcination temperature of the tungstated zirconia support was optimized to be 700 °C, which gives optimal results in terms of surface area, surface acidity, and catalytic performance in the SCR reaction. Zirconia support promoted with the tungsten oxide is further labelled as WZ_AH, with AH corresponding to the precipitating agent ammonium hydroxide.

The same zirconyl precursor was applied for the synthesis of SO_4^{2-}/ZrO_2, but ethylene diamine was used as a precipitator instead of aqueous ammonia, resulting in zirconia with a higher surface area. According to D'Souza et al. [19], ethylene diamine most likely acts as a bifunctional agent, both precipitating the zirconyl to hydrous zirconia and also functioning as

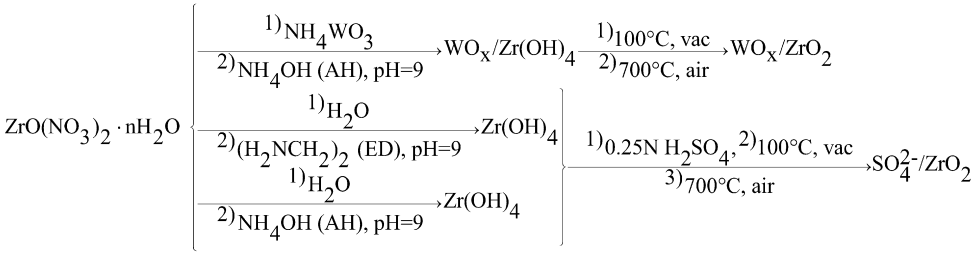

Scheme 1.

a colloidal protecting agent for the $Zr(OH)_4$ domains. Several samples were also prepared with ammonium hydroxide as precipitating agent, to compare the effect of precipitants.

For the synthesis of SO_4^{2-}/ZrO_2, 66.9 g $ZrO(NO_3)_2{\cdot}nH_2O$ was dissolved in 700 mL of water at room temperature. When the zirconyl precursor was dissolved, 75 mL of ethylene diamine was added slowly during stirring, followed by precipitation of hydrous zirconia. The stirring was continued overnight at 50 °C, followed by heating for 1 week at ∼65 °C, to avoid decomposition of ethylene diamine (boiling point 117 °C). After this, two phases were present: a clear slightly yellow liquid at the top indicating an excess of ethylene diamine and the precipitated hydrous zirconia in the bottom fraction. The slurry was filtered and washed with about 1000 mL of water in a Büchner funnel and dried in vacuum oven overnight at 100 °C and 10 mmHg. The resulting xerogel was sulfated, based on an optimized procedure from Gonzalez et al. [21]. Freshly prepared $Zr(OH)_4$ was immersed overnight in a 0.25 N H_2SO_4 solution, 15 mL/g. Then the mixture was suction filtered, washed with a small amount of 0.25 N H_2SO_4 (0.125 M) and dried in a vacuum oven at 100 °C overnight. All promoted supports were calcined at 700 °C for 4 h in air. The short calcination time minimized the decomposition of sulfate at elevated temperatures.

The supported V-based catalysts were prepared by impregnating the support with an aqueous solution of ammonium vanadate to obtain a vanadium loading of 1.7 wt% (3.0 wt% V_2O_5). The incipient wetness method was used for impregnation. After impregnation, the samples were dried for 2 h at 100 °C and calcined for 3 h at 400 °C in air.

The potassium-poisoned catalysts were prepared by impregnation with a solution of KNO_3 to obtain a potassium loading of 134 μmol/g, corresponding to a K/V molar ratio of 0.4. Samples were then dried in air at 100 °C and calcined at 300 °C. The K-doped, vanadium-impregnated sulfated zirconia samples are designated KVSZ_AH or KVSZ_ED, where AH and ED indicate the precipitating agent ammonium hydroxide and ethylene diamine, respectively.

2.2. Nitrogen adsorption measurements

Nitrogen adsorption measurements were performed at liquid nitrogen temperature using a Micromeritics Gemini analyzer. The samples were evacuated at 200 °C for 1 h before the measurements. The total surface area was calculated according to the BET method.

2.3. Thermogravimetric analysis coupled with mass spectroscopy

Simultaneous thermogravimetric analysis (TGA) and mass spectroscopy (MS) of the gases evolved from the sulfated zirconia sample were performed using a TGA–MS system that includes a NETZSCH STA 409 PC/PG and a NETZSCH QMS 403 C mass spectrometer. The samples were purged with N_2 and scanned from 20 to 1200 °C, with a temperature ramp rate of 20 °C/min.

2.4. X-ray powder diffraction

Room-temperature X-ray powder diffraction (XRPD) measurements were performed on a Philips PW 1820/3711 powder diffractometer using CuK_α radiation ($\lambda_1 = 1.5406$ Å/1.5443 Å) with a range of 10–65° in steps of 0.02° in 2θ. In situ high-temperature XRPD was carried out at beamline I711 at the MAXII synchrotron, MAX-lab, Lund, Sweden, on a Huber G670 imaging strip Guinier camera, using a wavelength of $\lambda_2 = 1.154424(8)$ Å. The data were accumulated for 60 s in the range of 4–100° in steps of 0.005° in 2θ. For easy comparison, the angle of the latter is converted by applying Braggs law: $\theta_1 = \arcsin((\lambda_1/\lambda_2)\sin\theta_2)$, where θ_2 is the angle corresponding to the data obtained with the wavelength 1.154424 Å.

2.5. In situ Raman spectra

A homemade Raman cell was used for recording the in situ Raman spectra of the studied catalysts consisting of a double-walled quartz-glass transparent tube furnace mounted on a xyz plate, allowing it to be positioned on the optical table. The inner furnace tube (23 mm o.d., 20 mm i.d., and 10 cm long) is Kanthal wire-wound for heating the cell. The cell has a gas inlet and a gas outlet, as well as a thermocouple sheath with a sample holder at its tip. Approximately 180 mg of each catalyst was pressed into a wafer and mounted on the holder that could be vertically adjusted in the in situ cell.

The gases used were O_2 (L'Air Liquide 99.995%), 10,000 ppm NH_3/N_2 and 10,000 ppm NO/N_2 mixtures (L'Air Liquide) and N_2 (L'Air Liquide 99.999%) as balance gas. The gas feed consisted of 2000 ppm NO, 2200 ppm NH_3 ($NH_3/NO = 1.1$), and 7% O_2 balanced in N_2 or various mixtures of these at a total feed flow rate of up to 50 mL/min. To study the effect of H_2O(g) on the in situ Raman spectra, the dry feed gas was enriched by 3% H_2O(g) as described earlier [22].

The 488.0-nm line of a Spectra Physics Stabilite 2017 Ar^+ laser was used for recording of the Raman spectra. The laser beam, operated at 40 mW, was focused on the sample by a cylindrical lens, thus dispersing it to reduce sample irradiance. The scattered light was collected at 90°, analyzed with a 0.85-m Spex 1403 double monochromator, and detected by an RCA PMT cooled to −20 °C equipped with EG&G photon-counting electronics. The entire setup is illustrated in Fig. 1.

Recording of spectra started in O_2 at 400 °C (dehydrated conditions) after the sample was exposed for 1 h at 400 °C in pure O_2. Raman spectra were then recorded sequentially after stabilization for 1 h in $NH_3/H_2O/N_2$ (reductive), $NH_3/NO/O_2/H_2O/N_2$ (NO-SCR operational), and finally in O_2 (reoxidation) at 400 °C.

2.6. NO SCR with ammonia

Before the activity measurements, samples where pressed into tablets, crushed, and sieved to obtain fractions of 0.18–0.295 mm. The SCR activity measurements were carried out in a fixed-bed reactor, with 75 mg of the catalyst loaded between

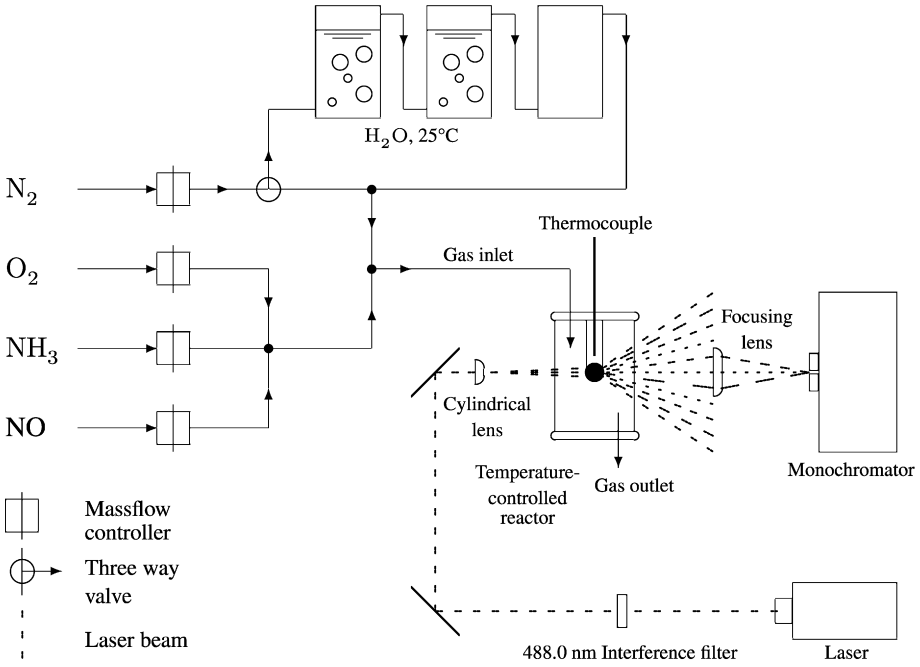

Fig. 1. Schematic illustration of the in situ Raman setup.

two layers of inert quartz wool. The typical reactant gas composition was 1000 ppm NO, 1100 ppm NH_3, 3.5% O_2, 2.3% H_2O, and balance N_2. The total flow rate was maintained at 300 mL/min (ambient conditions). The NO concentration was continuously monitored by a Thermo Electron model 10A rack-mounted chemiluminescent NO–NO_x gas analyzer.

The catalytic activity, represented as a first-order rate constant (k), can be calculated from the NO conversion, X, as

$$k = -\frac{F_0}{[\mathrm{NO}]_0 \cdot V_{\mathrm{cat}}} \ln(1 - X),$$

where F_0 is the molar inflow of NO, $[\mathrm{NO}]_0$ is the initial molar concentration of NO, and V_{cat} is the volume of the catalyst bed.

2.7. NH_3 temperature-programmed desorption

Temperature-programmed desorption of ammonia (NH_3-TPD) was performed as follows. First, 100 mg of the sample was loaded into a quartz tube reactor and saturated with ammonia (100 mL/min, 1% NH_3/N_2) for 45 min at room temperature. Before the NH_3 desorption measurement, the sample was heated to 100 °C in a dry nitrogen flow (100 mL/min) and kept at this temperature for 1 h to remove physisorbed ammonia. Then the sample was cooled to 50 °C, after which the temperature was raised at a rate of 5 °C/min up to 650 °C. The rate of NH_3 desorption was monitored by a computer-interfaced Jasco V-570 UV/VIS/NIR spectrophotometer using the characteristic ammonia band at 201 nm.

2.8. Computational methods

Energy minimization was performed using the hybrid density functional B3LYP [23–25], in combination with the LACVP* basis set as incorporated in the Jaguar program package [26]. The LACVP* basis set uses the Los Alamos effective core potential (ECP) and basis set for the description of heavy atoms (V, K) [27], whereas all lighter atoms (O, C, H) are described using the 6-31G* basis set [28]. The ECP was augmented with an explicit treatment of the outermost core electrons and valence electrons, resulting in the electron configurations $[\mathrm{core}]3s^2 3p^6 3d^4 4s^1$ for vanadium and $[\mathrm{core}]3s^2 3p^6 4s^1$ for potassium. For the obtained minimum energy structures, Mulliken charges [29] and charges fitted from the electrostatic potential (ESP) [30–32] were calculated to characterize the interactions among V, O, and K^+.

Analytical frequencies were calculated for all structures, which allowed derivation of thermodynamic properties at $T = 298$ K. The reported frequencies were scaled using a scaling factor of 0.9614, which is the appropriate scaling factor for the B3LYP/6-31G* method [33].

3. Results and discussion

3.1. Surface area and vanadium surface coverage

The results of the BET surface area measurements for samples prepared using different precipitating agents are summarized in Table 1. It is noticeable that the use of ethylene diamine as precipitant resulted in a roughly twofold higher specific surface area for the ZrO_2 carrier compared with the samples prepared with ammonium hydroxide as a precipitant. In addition, the use of different precipitating agents during preparation of the sulfated carrier (SO_4^{2-}/ZrO_2) resulted in materials of 2- to 3-fold greater surface areas compared with the corresponding nonsulfated carrier. Incorporation of tungsta in zirconia (tungstated zirconia supports) resulted in materials with nearly 2-fold higher specific surface areas compared with the

Table 1
Sample characteristics[a]

Catalyst sample	S_{BET} (m^2/g)	n_s (VO_x/nm^2)	n_s (WO_x/nm^2)	NH_3 des. (μmol/g)
SZ_ED	118.0			375
VZ_ED	51.6	3.9		
KVZ_ED	50.2	4.0		
VSZ_ED	102.9	2.0		551
KVSZ_ED	97.0	2.1		363
VZ_AH	23.4	8.6		
WZ_AH	94.7		5.5	253
VWZ_AH	58.4	3.4	8.9	351
KVWZ_AH	57.9	3.5	9.0	191
SZ_AH	84.8			354
VZ_AH	23.4	8.6		
KVZ_AH	21.6	9.3		
VSZ_AH	71.9	2.8		516
KVSZ_AH	66.6	3.0		292
VWT_ref	68.3	2.9	2.7	
KVWT_ref	62.7	3.2	2.9	

[a] All vanadia-containing samples are loaded with 1.7 wt% vanadium. For samples doped with potassium, K/V = 0.4 (molar ratio).

corresponding nontungstated samples (Table 1). The increased surface area would be expected to lead to better dispersion of the active components and lower values for the vanadium surface coverage, n_s (VO_x/nm^2), where the saturation value for the monolayer surface coverage of vanadium was reported to be approximately 8 VO_x/nm^2 [34].

3.2. Thermogravimetric analysis and mass spectroscopy

The results of TGA–MS for the sulfated $Zr(OH)_4$ xerogel samples precipitated with ED and AH and dried at 100 °C are presented in Fig. 2. The TGA curve of the sulfated zirconia xerogel contains at least two weight loss features. The first, below 200 °C with $m/e = 18$ response in the MS signal, is attributed to desorption of physisorbed water. The second, between 400 and 1000 °C, with MS signals of $m/e = 64$ and 32, can be attributed to desorption of sulfate species in the form of SO_2 and O_2, respectively.

A particular difference between the two samples was observed regarding the temperature of surface sulfate species decomposition, indicating that the preparation method influenced the stability of these species. In the case of VSZ_AH, the $m/e = 64$ signal was observed at temperatures above 700 °C, whereas for the VSZ_ED, decomposition of the sulfate species proceed in two steps at temperatures around 400–500 °C and 500–900 °C. Desorption of a small amount of water and SO_2 was observed for the ED-precipitated sample at around 400–500 °C, which could be connected to the decomposition of H_2SO_4 or hydrated sulfate species.

The stability of the sulfate species was somewhat higher on the AH-precipitated samples, reflected by the ∼200 °C higher temperature of SO_2 desorption for the AH-precipitated sample compared with the corresponding ED-precipitated sample. This could be due to differences in the textural properties (i.e., surface acidity, porosity) related to the precipitating agent.

Table 2
Atomic fractional coordinates for the phases used in the Rietveld refinements. The space group $P2_1/n$ is only applied for the samples containing tungsten oxide

Atom	Fractional coordinates		
	x	*y*	*z*
tet-ZrO_2 ($P4_2/nmc$)			
Zr	0.750	0.250	0.750
O	0.250	0.250	0.800
mon-ZrO_2 ($P2_1/c$)			
Zr	0.276	0.040	0.209
O1	0.072	0.333	0.347
O2	0.449	0.758	0.476
cubic-ZrO_2 (Fm3m)			
Zr	0.000	0.000	0.000
O1	0.250	0.250	0.250
mon-WO_3 ($P2_1/n$)			
W1	0.252	0.026	0.285
W2	0.247	0.033	0.781
O1	0.000	0.025	0.220
O2	0.000	0.475	0.220
O3	0.290	0.290	0.265
O4	0.210	0.290	0.735
O5	0.280	0.040	0.030
O6	0.280	0.240	0.000

Integration of the SO_2-desorption signals for the AH- and ED-precipitated samples (Fig. 2) revealed an approximately 33% higher SO_2-desorption area for the ED-precipitated samples. VSZ_ED (102.9 m^2/g) exhibited a 43% greater surface area than VSZ_AH (71.9 m^2/g). This suggests that the amount of sulfate on the samples is, to some extent, proportional to the surface area.

3.3. XRD and phase compositions

The temperature used for calcination of the sulfated zirconia samples was based on results from temperature-programmed XRD, depicted in Fig. 3. At 700 °C, a maximum in the amount of tetragonal ZrO_2-phase was observed, which has been suggested to be necessary for the generation of high acidity in sulfated zirconia [35,36]. This phase remains stable during cooling, as can be seen in Fig. 3 (right). The periodic variations in the intensities are due to instabilities in the beamline.

The XRD patterns of selected samples were refined with the Rietveld refinement method, as shown in Fig. 4. All of the samples were composed of three crystal phases with different positions of zirconium and oxygen atoms and bond lengths. The unit cell symmetries can be described by the space groups $P4_2/nmc$, $P2_1/c$, and Fm3m, corresponding to the tetragonal, monoclinic, and cubic ZrO_2 phases ($P2_1/n$ for WO_3-containing samples), with atoms in the positions specified in Table 2. This unit cell was used in the model of the XRD pattern for refining the crystalline structures with the Rietveld method. The results of the refinements of the crystalline phases are summarized in Table 3. Through the refined XRD patterns, it is possible to comment on the effect of the sulfation and the precipitant on the crystal form and crystallinity of the zirconia matrix.

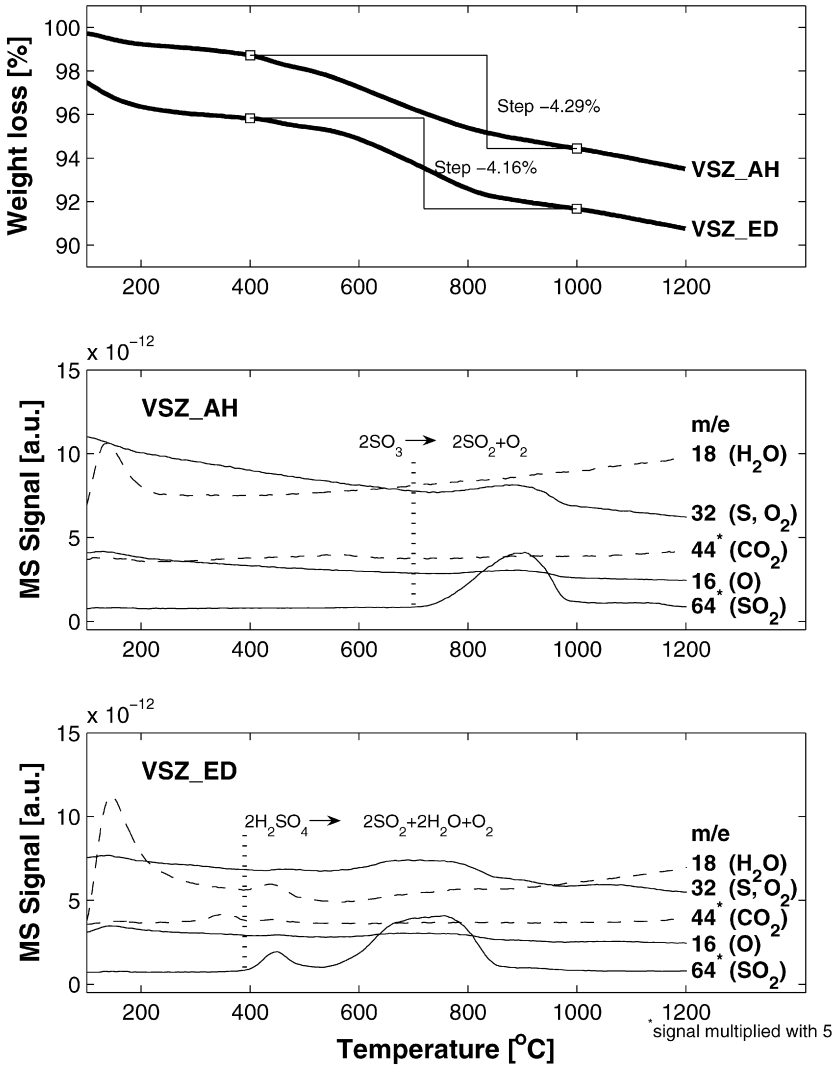

Fig. 2. Thermogravimetric and mass spectral analysis of the vanadium-impregnated sulfated zirconia samples, precipitated with two different agents, AH (ammonium hydroxide) and ED (ethylene diamine).

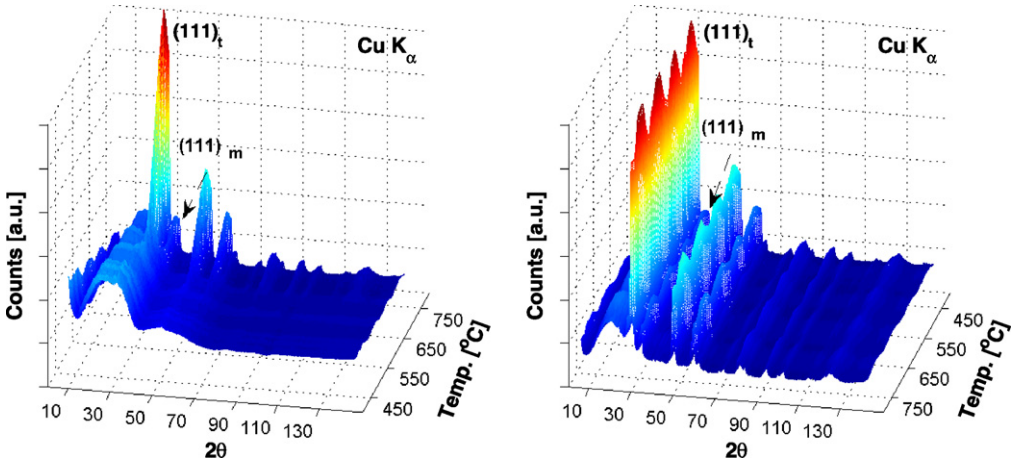

Fig. 3. X-ray diffraction of $SO_4^{2-}/Zr(OH)_4$ heating from 450–700 °C with 10 °C steps (left), and cooling (right). The zirconia reflex of the $(111)_t$ and $(111)_m$ is indicated.

The difference in SO_2-desorption temperature observed in the TGA–MS spectra (Fig. 2) also can be connected with the distinction in crystallographic composition of ZrO_2 and the resulting difference in coordination strength of sulfate to the support. Rietveld refinements suggested a higher amount of monoclinic zirconia of the AH-precipitated samples (Table 3).

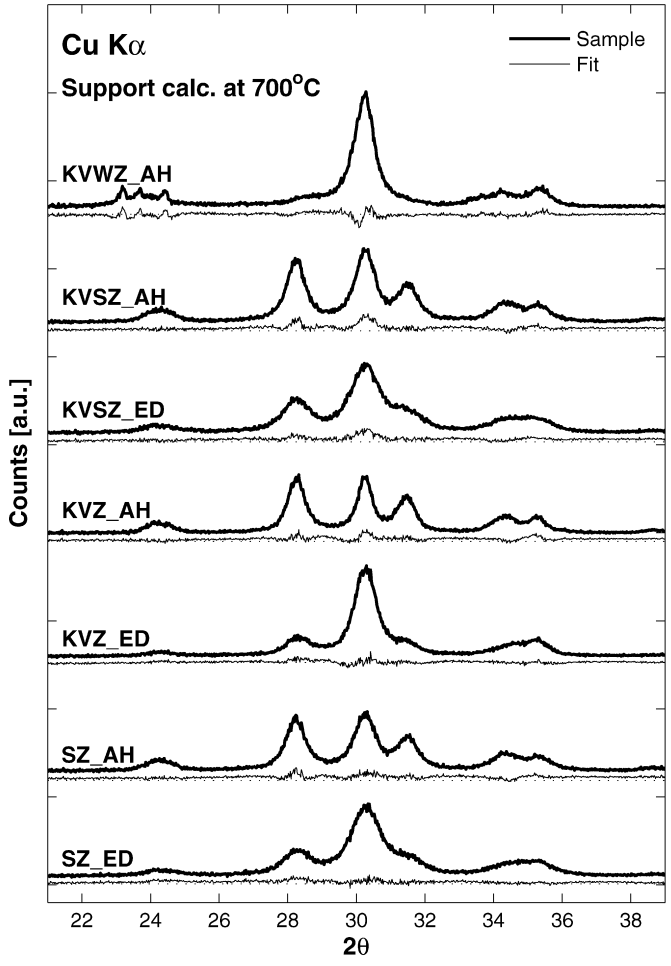

Fig. 4. Rietveld refinement of the XRD data of sulfated and tungstated zirconia samples, precipitated with AH or ED, all calcined at 700 °C in air. The difference between the observed and calculated intensities is shown at the lower curve below the corresponding profile.

Although not studied further in this work, this implies that the m-ZrO_2 may be responsible for the relatively stronger binding of sulfate species.

3.3.1. Precipitant effects

Comparison of different ED-precipitated samples (i.e., SZ_ED, KVZ_ED, and KVSZ_ED in Table 3) indicates that the presence of sulfate, vanadia, and potassium have a negligible effect on the crystallinity of the ZrO_2 matrix, which in all cases is >70%. The phase composition of the crystalline fraction consists mostly of tetragonal ZrO_2. Several studies have proposed that the ZrO_2 tetragonal phase is more active in catalysis, and it also has been reported to be responsible for the generation of high acidity [35,36].

The samples precipitated with AH also exhibited high crystallinity (>70%), whereas about 50 vol% (of the crystalline fraction) was calculated to exist as tetragonal or cubic zirconia. The higher amount of tetragonal phase in the ED-precipitated samples can be explained if we suggest that the phase transformation from tetragonal to the thermodynamically more stable monoclinic ZrO_2 is retarded to a higher degree for the ED-precipitating agent than for AH. This can be explained by the stabilizing effect of the ED in the zirconia matrix, as proposed by Richards et al. [19]. These authors suggested a colloidal protecting effect of ethylene diamine, which hinders the hydrous zirconia particles from sintering. This stabilizing effect of ED could thus retard the phase transformation from tetragonal to monoclinic zirconia. Comparing the effect of AH or ED precipitants on the SZ, KVZ, and KVSZ samples reveals that in all cases, precipitating with AH resulted in a significantly higher amount of monoclinic ZrO_2 phase.

Table 3
Crystallinity and the calculated volumetric distribution of ZrO_2 (and WO_3) phases from Rietveld refinement

Sample	Crystallinity[a] (%)	V_{WO_3} (vol%)	$V_{tet+cubic}$ (vol%)	V_{mon} (vol%)
KVWZ_AH	68.8	9.2 (0.2)	83.5 (1.6)	7.3 (0.4)
KVSZ_AH	76.1	–	51.4 (1.8)	48.6 (0.9)
KVSZ_ED	71.4	–	59.3 (1.8)	40.7 (0.9)
KVZ_AH	72.3	–	48.4 (2.1)	51.6 (1.1)
KVZ_ED	74.7	–	75.2 (2.6)	24.8 (1.2)
SZ_AH	72.2	–	54.8 (2.2)	45.2 (1.0)
SZ_ED	76.5	–	61.4 (2.3)	38.6 (1.3)

[a] Integration over (observed pattern − refined background pattern)/observed pattern.

A similar comparison could not be performed for the coprecipitated WZ samples, due to the necessary washing step when precipitating with ED. The washing would remove a significant part of the coprecipitated tungsten oxide. However, tungsten oxide is known to have a similar retarding effect on the transformation from tetragonal to monoclinic zirconia [20]. Therefore, tungstated samples are assumed to consist exclusively of tetragonal ZrO_2 phase.

3.3.2. Effect of sulfate

It is generally agreed that sulfation retards crystallization of the zirconia matrix and thus the transformation from tetragonal to monoclinic form [37]. The incorporation of sulfate species into the $Zr(OH)_4$ structure presumably stabilizes the tetragonal zirconia phase by shifting the equilibrium phase distribution from the thermodynamically more stable monoclinic to the metastable tetragonal phase. However, in our studies, we observed that doping the zirconia matrix with sulfate seemed to favor the formation of monoclinic ZrO_2 after calcination at 700 °C. Comparing the fraction of monoclinic ZrO_2 for KVZ_ED and two sulfated samples KVSZ_ED and SZ_ED (Table 3) showed that the share of monoclinic phase increased from 24.8 to 40.7 and 38.6 vol%, respectively, after sulfation.

Sulfation of AH-precipitated samples seemed to have less impact on the generation of a specific crystal phase. Sulfating the KVZ_AH samples resulted in an insignificant increase in tetragonal zirconia phase from 48.4 to 51.4 vol% for KVSZ_AH.

3.3.3. Tungstated zirconia

The XRD pattern of KVWZ_AH displayed three crystalline phases, two zirconia phases, and one monoclinic WO_3 phase (Fig. 4), with no crystalline vanadium or potassium oxides ob-

served due to their low loadings. The incorporation of tungsten oxide into the zirconia matrix is known to stabilize the tetragonal crystal phase over the monoclinic form [15,20]. This tendency can be clearly seen when calculating the contribution of different ZrO_2-phases, with 83.5 vol% of the crystalline zirconia existing as tetragonal and only 7.3 vol% existing as monoclinic. (Note that the values are not normalized to the presence of crystalline WO_3.) The appearance of crystalline tungsten oxide for the sample calcined at 700 °C can be attributed to the low surface area and thus a high surface concentration of WO_3 species, far exceeding monolayer coverage.

3.4. In situ Raman spectra and structural characteristics of catalysts

3.4.1. Effects of sulfation of the zirconia support and K poisoning of catalysts

Fig. 5 shows the in situ Raman spectra obtained at 400 °C under a flow of oxygen for representative samples prepared using ethylene diamine as the precipitant during the zirconia support synthesis step. It should be pointed out that the preparation procedure resulted in mixtures of tetragonal and monoclinic zirconia phases and that the Raman spectra were dominated by the spectral characteristics of the phase formed in excess. Spectrum 5(a) has a characteristic band at 636 cm^{-1}, corresponding to tetragonal ZrO_2 [20] (ED-precipitated, calcined at 700 °C). In agreement with the results of XRD analysis, the addition of sulfuric acid in the precursor solution during the preparation of the sulfated zirconia (SO_4^{2-}/ZrO_2; spectrum Fig. 5b) resulted in the formation of a higher concentration of monoclinic ZrO_2 (band at 622 vs 636 cm^{-1} for the tetragonal phase). The formation of surface sulfate species also was visible in the Raman spectra. The Raman bands due to the surface sulfates probably originated from two kinds of surface sulfate species. The bands at 994 cm^{-1} and 1035 cm^{-1} in Fig. 5b observed in the expected range of ν_1 and ν_3 SO_4^{2-} modes probably correspond to the sulfate groups connected in a bidentate coordination to the carrier. The band at 1394 cm^{-1} is assigned to the S=O stretching mode of a surface tridentate sulfate with a (Zr–O)$_3$–S=O configuration [38,39]. The Raman spectrum of the V_2O_5/ZrO_2 (1.7VZ_ED) sample (Fig. 5c) exhibited the known [40] features of surface amorphous vanadates, that is, isolated tetrahedral-like monomeric and polymeric vanadates (Zr–O)$_3$–V=O. The band at ∼1030 cm^{-1} is due to V=O stretching and the broad band in the 700–940 cm^{-1} region, centered around 760 cm^{-1}, is due to V–O–V structures. The weak narrow band at 993 cm^{-1} indicates the presence of traces of V_2O_5 bulk particles. Such V_2O_5 particles with distorted VO_5 coordination can be present even in catalysts with submonolayer coverage (4 VO_x/nm^2 in this sample, slightly above half monolayer) and are not detectable by XRD. These particles can be dispersed into amorphous state by subjecting the catalyst to the reaction mixture [34]. Indeed, after the V_2O_5/ZrO_2 catalyst was exposed to a flow of $NH_3/H_2O/N_2$ and subsequent reoxidation, the band at 993 cm^{-1} nearly disappeared.

We now focus on the effect of sulfation. Comparing the spectra of the V_2O_5–SO_4^{2-}/ZrO_2 (VSZ_ED) catalyst (Fig. 5e) and

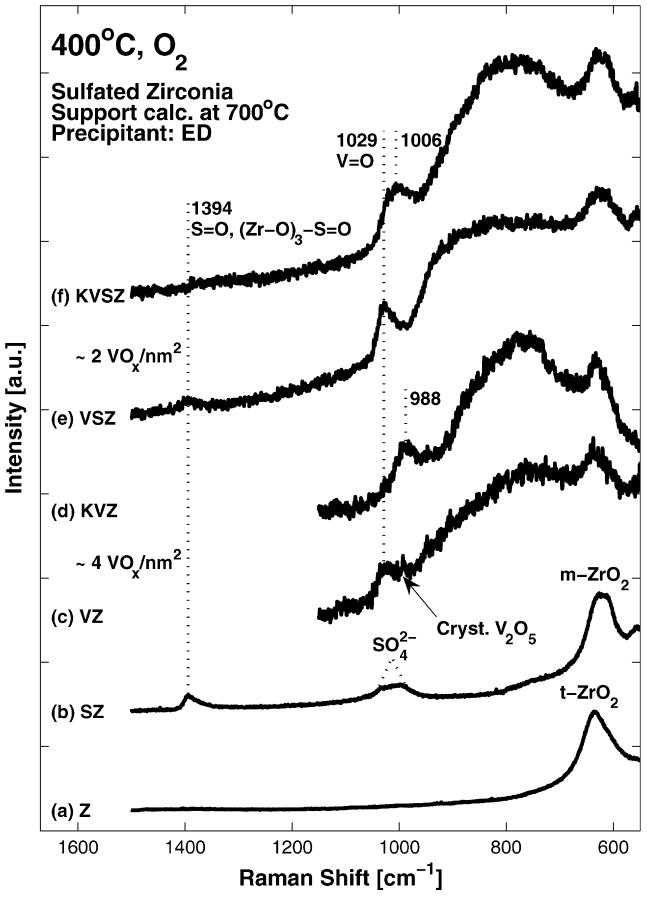

Fig. 5. In situ Raman spectra of catalyst samples recorded under O_2 at 400 °C: (a) ZrO_2; (b) SO_4^{2-}/ZrO_2; (c) $1.7V_2O_5/ZrO_2$; (d) K_2O–$1.7V_2O_5/ZrO_2$; (e) $1.7V_2O_5$–SO_4^{2-}/ZrO_2; (f) K_2O–$1.7V_2O_5$–SO_4^{2-}/ZrO_2. Laser wavelength, $\lambda_0 = 488.0$ nm; laser power = 40 mW, scan rate = 0.07–0.3 $cm^{-1}s^{-1}$; spectral slit width = 8 cm^{-1}.

the V_2O_5/ZrO_2 sample (Fig. 5c) leads to the following observations:

(i) The band at 993 cm^{-1} due to V_2O_5 particles was not observed in the spectrum of the V_2O_5–SO_4^{2-}/ZrO_2 catalyst (Fig. 5e). This is due to the fact that sulfation of the support resulted in a significantly greater surface area (S_{BET} = 102.9 m^2/g) and correspondingly lower vanadium surface coverage (n_s = 2.0 VO_x/nm^2) compared with V_2O_5/ZrO_2 (n_s = 3.9 VO_x/nm^2); therefore, vanadia was dispersed only in the form of amorphous vanadates. Decreasing the V surface coverage also resulted in a higher signal-to-noise ratio, due to lower absorption of the incident laser light by the sample surface.

(ii) The peak related to the V–O–V mode was blue-shifted for the V_2O_5–SO_4^{2-}/ZrO_2 catalyst (Fig. 5e) and appeared to be centered at ca. 900 cm^{-1}, compared with ca. 760 cm^{-1} in the spectrum of V_2O_5/ZrO_2 catalyst (Fig. 5c). According to a recent study [17], such spectral behavior has significant structural implications and is compatible with a small amount of V–O–V chains consisting of polyvanadates. We discuss this last point in more detail later.

(iii) The position of the V=O mode at 1030 cm^{-1} remained unaffected.

The effect of K poisoning on the Raman spectra of the catalysts can be examined by comparing the spectrum of the K–V_2O_5/ZrO_2 (K–1.7VZ_ED) catalyst (Fig. 5d) to the spectrum of the V_2O_5/ZrO_2 sample (Fig. 5c) and by comparing the spectra of the K–V_2O_5–SO_4^{2-}/ZrO_2 (K–1.7VSZ_ED) catalyst (Fig. 5f) and the V_2O_5–SO_4^{2-}/ZrO_2 sample (Fig. 5e). The following observations can be made:

(i) The band of the tridentate surface sulfate, (Zr–O)$_3$–S=O, at 1394 cm^{-1} S=O was not present in the spectrum of the K-poisoned sulfated catalyst (Fig. 5f).
(ii) The V=O band was red-shifted from ∼1030 to ∼990 cm^{-1} for K–V_2O_5/ZrO_2 (spectrum in Fig. 5d) and to ∼1005 cm^{-1} for K–V_2O_5–SO_4^{2-}/ZrO_2 (spectrum in Fig. 5f).
(iii) The peak related to the V–O–V functionalities was red-shifted, and its intensity was enhanced relative to that at 630 cm^{-1} in both K-doped samples. In particular, the high-frequency wing almost disappeared on going from spectrum c to spectrum d, and the center of the broad peak was red-shifted by ∼80 cm^{-1} (from ∼900 to ∼820 cm^{-1}) on going from spectrum e to spectrum f.

It is evident that the simultaneous presence of K_2O and sulfate groups dispersed on the surface can result in the formation of potassium sulfate, thereby contributing also to enlargement of the band at ∼1000 cm^{-1} (where the main stretching band for the sulfate group is expected) in the spectrum of the K–V_2O_5–SO_4^{2-}/ZrO_2 sample (Fig. 5f). Moreover, as has been suggested by Bulushev et al. [12], potassium could, through an electrostatic interaction, (Zr–O)$_3$–V=O$^{\delta-}\cdots$K$^{\delta-}$, cause an elongation of the V=O bond, thereby explaining the red shift observed for this band for the K-poisoned samples. Another explanation of the decreased red shift of the V=O band on K-doping the V_2O_5–SO_4^{2-}/ZrO_2 sample (∼1006 cm^{-1}; Fig. 5f) compared with K–V_2O_5/ZrO_2 (988 cm^{-1}; Fig. 5d) could be attributed to the presence of sulfate species, leaving the V=O sites less affected by the interaction with potassium. The red shift of the V–O–V band indicates a weakening of the bridging V–O bonds and could be a result of the formation of $(VO_x)_n$ units with a higher degree of polymerization, as we discuss later. Finally, it has been proposed that some of the O=V–O–support anchoring bridges can be substituted by O=V–O–K [41], which also could contribute to elongation of the V=O bond.

3.4.2. *In situ Raman spectra of V_2O_5–WO_3/ZrO_2 catalysts*

Fig. 6 shows the in situ Raman spectra obtained at 400 °C under a flow of O_2 for representative samples prepared using ammonium hydroxide as precipitant in the zirconia support synthesis step. Fig. 6a corresponds to monoclinic ZrO_2 and has a characteristic band at 637 cm^{-1} [20]. In situ Raman spectrum of the mixed WO_3/ZrO_2 support material, synthesized by coprecipitation as described earlier, is shown in Fig. 6b. The bands observed are characteristic of dispersed surface amorphous polytungstate species: a strong sharp band due to W=O stretching at 1019 cm^{-1} originating from mono-oxo species [42] and broad bands at ∼910 and 825 cm^{-1} occurring in the asymmetric W–O–W stretching region. No bands due to crystalline WO_3 can be observed, indicating very good dispersion of surface tungstates and nearly complete coverage of zirconia. The surface coverage of the sample, 5.5 WO_x/nm^2, slightly exceeded the experimentally reported monolayer (4 WO_x/nm^2 [42]). It is possible that tungstates remained trapped in the inner pores of the support as a result of the applied synthesis route. The Raman spectrum shown in Fig. 6b is in agreement with previously reported spectra for WO_x/ZrO_2 samples [43,44] and is characteristic of a sample with high tungsta loading not exceeding the monolayer coverage. The structure of surface tungsta species on metal oxide supports is a function of WO_x coverage [42], and multiple geometrical configurations for polytungstates with varying bond orders for bridging W–O–W bonds (spectral region 800–950 cm^{-1}) occur at the surface for the samples with high tungsten loadings [44].

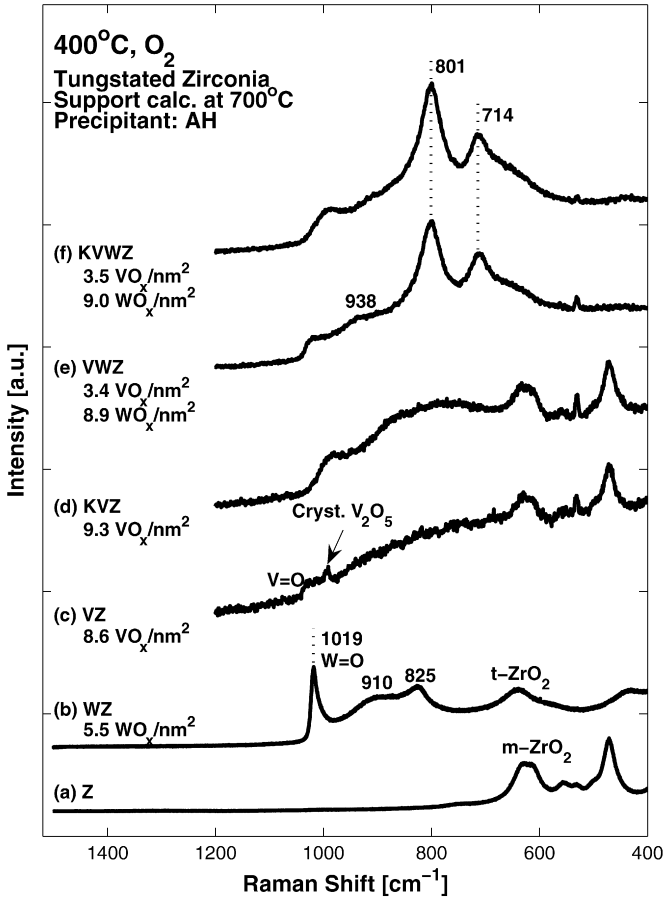

Fig. 6. In situ Raman spectra of catalyst samples recorded under O_2 at 400 °C: (a) ZrO_2; (b) WO_3/ZrO_2; (c) 1.7V_2O_5/ZrO_2; (d) K_2O–1.7V_2O_5/ZrO_2; (e) 1.7V_2O_5–WO_3/ZrO_2; (f) K_2O–1.7V_2O_5–WO_3/ZrO_2. Recording parameters: See Fig. 5 caption.

The spectrum obtained for the V_2O_5/ZrO_2 (VZ_AH) sample is shown in Fig. 6c. Due to the lower BET area of this sample (23.4 m^2/g) compared with the sample prepared using ED as precipitant (51.6 m^2/g), and its correspondingly higher surface VO_x coverage (8.6 VO_x/nm^2), the saturation value for the

surface VO_x monolayer (~8 VO_x/nm^2) was exceeded, and the band at 993 cm^{-1} due to crystalline V_2O_5 can be clearly seen in spectrum in Fig. 6c. The remaining features observed in spectrum in Fig. 6c (i.e., the band at ~1030 cm^{-1} due to V=O and the very broad V–O–V band at 800–930 cm^{-1}) are characteristic of surface amorphous vanadates in the catalysts with high vanadium loading.

The effect of tungstation can be revealed by comparing spectrum in Fig. 6e obtained for the V_2O_5–WO_3/ZrO_2 sample (VWZ_AH) with the spectrum in Fig. 6c obtained for the corresponding V_2O_5/ZrO_2 (VZ_AH) sample. Two very intense bands at 714 and 801 cm^{-1} dominate in spectrum in Fig. 6e and are characteristic of crystalline WO_3 [45]. The positions and shapes for these bands are known to be dependent on the crystallite size and temperature [45]. It is evident that deposition of vanadia on WO_3/ZrO_2 resulted in the "extraction" of amorphous $(WO_x)_n$ and a redistribution of a significant portion of surface tungsta in the form of crystalline WO_3. The rest of the features in Fig. 6e are largely obscured by the envelopes of the above bands and appear to consist of overlapping contributions from bands due to noninteracting surface amorphous vanadates and tungstates at ~1020 cm^{-1} (M=O region) and ~940 cm^{-1} (M–O–M region). Earlier work [46] has demonstrated that noninteracting surface vanadates and tungstates are also formed on TiO_2.

The effect of K poisoning is similar to that discussed in the context of Fig. 5 for sulfated supports, that is, elongation of the M=O bonds (red shift of the band at ~1020 cm^{-1} in the spectrum in Fig. 6e to ~990 cm^{-1} in the spectrum in Fig. 6f) and reorganization of polyvanadates and polytungstates to species with weaker M–O–M bridging bonds. The band at 940 cm^{-1} in the spectrum in Fig. 6e was red shifted and presumably covered under the envelope of the 801 cm^{-1} WO_3 band in spectrum in Fig. 6f.

3.4.3. Raman band assignments and structural implications

The molecular configurations for surface vanadates in supported vanadia catalysts under dehydrated conditions evolve from isolated monovanadates and larger polyvanadates with tetrahedral coordinated vanadium [47] at low vanadium coverage to bulk V_2O_5 when the monolayer coverage of the support is exceeded. Fig. 7 shows molecular models for possible configurations of the isolated and polymeric amorphous surface vanadates. Here we attempt to correlate the effect of the various preparation steps (e.g., choice of precipitant, sulfation, and K-doping) as expressed in the Raman spectra with the response of the particular structure of the dispersed vanadia phase.

The consistency of the Raman assignments can be checked using the following empirical correlations between V–O Raman stretching frequencies and the corresponding V–O bond lengths and Pauling bond strengths [48]:

$$\nu = 21349\exp(-1.9176R), \tag{1}$$

$$\mathrm{BO} = \left(0.2912\ln(21349/\nu)\right)^{-5.1}, \tag{2}$$

where ν is the V–O Raman stretching frequency (cm^{-1}), R is the corresponding bond length (Å), and BO is the Pauling bond

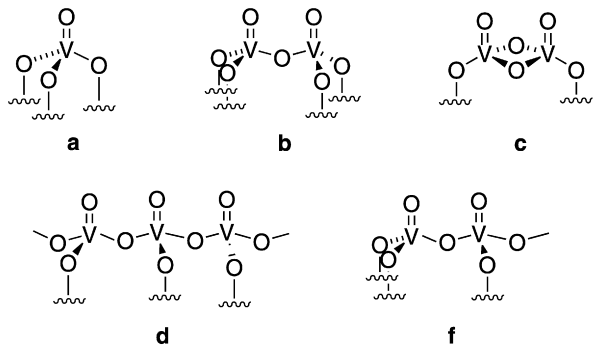

Fig. 7. Molecular models/configurations for monomeric (a), dimeric (b, c) and polymeric (d, e) dispersed surface vanadates.

strength in valence units (vu). According to the Pauling's valence sum rule, the sum of the individual V–O bond strengths for a viable configuration with four-coordinated vanadium for a vanadium oxide species should be equal to 5 vu [22,40,49]. This approach is based on the diatomic approximation, which is necessary for justifying the direct relationship between metal–oxygen bond lengths and Raman stretching frequencies [48]. As an example, we can calculate the bond orders for the surface isolated $(Zr–O)_3$–V=O species (configuration a in Fig. 7). The V=O band at 1029 cm^{-1} (Fig. 5c) corresponds to a bond order of 1.89 vu (1.581 Å), and the remaining 3.11 vu for the three V–O–Zr give rise to a BO close to unity (1.04 vu) for each V–O along the anchors.

Likewise, we can address the case of surface polyvanadates, for which the V–O–V functionalities exhibit a very broad band character (740–920 cm^{-1}) in the Raman spectra (Fig. 5c) due to the variation of V–O bond orders within geometrically related configurations for the $(VO_x)_n$ species. Band positions at ~900 and ~750 cm^{-1} imply bond orders of 1.51 and 1.14 vu, respectively. Thus, checking the viability of configuration b with one short V=O (1029 cm^{-1}, 1.89 vu) and one V–O–V (900 cm^{-1}, 1.51 vu), the valence units remaining for the two V–O(–Zr) bonds (determined from the constraint on the total bond order for the V atom) correspond to 0.8 vu for each V–O(–Zr). Configuration d also can be viable with one short V=O (1029 cm^{-1}, 1.89 vu) and two V–O–V (750 cm^{-1}, 1.14 vu), resulting in ca. 0.8 vu for the V–O(–Zr) bond ($5 - 1.89 - 2 \times 1.14 = 0.83$). It is evident that a V–O–V in the high-frequency edge (e.g., 900 cm^{-1}) is compatible with a small size for the $(VO_x)_n$ unit ($n = 2, 3$); if there were two V–O–V bridges per V (configurations c and d in Fig. 7) with the BO for each V–O around 1.5 vu, then there would remain no valence residue for the fourth (anchoring) V–O. Therefore, a red shift of the V–O–V functionalities indicates a reorganization of the surface polyvanadates in a form with longer chains and fewer anchoring V–O–Zr bridges per V. In contrast, a blue shift of the broad band is compatible with formation of smaller units with less V–O–V bridges per V.

In the K-doped V_2O_5/ZrO_2 sample (KVZ_ED; Fig. 5d) the V=O band was observed at 988 cm^{-1}, red-shifted from 1029 cm^{-1} (VZ_ED, Fig. 5c). The V=O band at 988 cm^{-1} corresponds to a bond strength of 1.79 vu. This suggests a weakening of the V=O bond order from 1.89 to 1.79 vu, length-

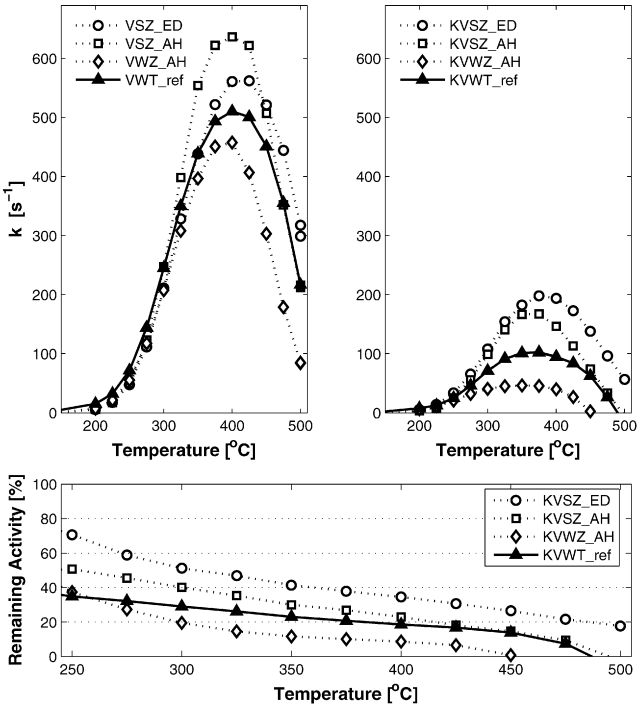

Fig. 8. The temperature dependency of the NO-SCR activity for the sulfate- and tungstate-promoted catalysts impregnated with 1.7 wt% vanadium (top left) and the corresponding potassium doped samples with a K/V molar ratio of 0.4 (top right). The effect of potassium on the SCR activity in the temperature range 250–500 °C is shown in the bottom as the remaining activity, defined by: $1 - [k_{\text{fresh}} - k_{\text{K-doped}}]/k_{\text{fresh}}$.

ened 0.02 Å (1.581 to 1.603 Å) when K-doping the V_2O_5/ZrO_2 sample.

3.5. NO-SCR activity measurements

The catalytic activity of the vanadia-impregnated samples promoted with tungsten oxide or sulfate were measured in the temperature range of 25–500 °C. The temperature dependency of the SCR activity is depicted in Fig. 8 for the supported vanadia catalysts before (Fig. 8, top left) and after doping with potassium oxide (Fig. 8, top right). The catalytic activity is represented as the first-order rate constant k. The activity of a commercial $3\%V_2O_5$–$7\%WO_x/TiO_2$ catalyst (VWT_ref) calcined at 450 °C is shown as a reference.

The vanadia-impregnated catalysts promoted with sulfate (1.7VSZ_AH and 1.7VSZ_ED) showed higher SCR activity compared with the corresponding tungstated catalyst (1.7 VWZ_AH, Fig. 8, top left). This is in accordance with the surface acidity given in Table 1, where the two sulfated catalysts had a significant higher surface acidity (516–551 μmol/g) than the tungstated catalyst (351 μmol/g), thus increasing the probability of formation of V–OH or Zr–OH Brønsted sites adjacent to V=O redox sites.

Previous studies of the effect of sulfation on the SCR activity of zirconia-based vanadia catalysts [14], also indicated that sulfation had a significant effect on the catalyst performance, increasing the activity up to 50% compared with that of the nonsulfated V_2O_5/ZrO_2 catalyst. Due to this and the fact that nonsulfated zirconia-based catalysts have a much lower alkali resistance [14], activity data for V_2O_5/ZrO_2 catalysts are not shown here.

The 1.7VSZ_AH and the 1.7VSZ_ED catalysts had very similar surface acidities but different surface areas (71.9 and 102.9 m^2/g, respectively) (Table 1). Thus, the relative proximity of the Brønsted and the V=O redox sites seems to be higher in the AH-prepared catalyst compared with the ED catalyst, explaining the somewhat higher activity of the former.

In all cases, doping the catalysts with potassium resulted in an overall decrease in catalytic activity combined with a shift in the maximum catalytic activity toward lower temperatures (Fig. 8, top right). A possible explanation for such a temperature shift is that the potassium loading reduced the activity of the main NO-SCR reaction while the rate of the side reaction of ammonia oxidation remained constant or even increased. The sulfate-promoted catalyst based on zirconia precipitated with ED displayed increased resistance to the alkali poisoning and was deactivated by only 58% at 350 °C, whereas the corresponding AH-precipitated, reference, and KVWZ catalysts were deactivated by 70%, 77%, and 88%, respectively. The catalyst resistance toward potassium poisoning seems to correlate well with the surface area and surface acidity (listed in Table 1), with VSZ_ED and VSZ_AH having the highest surface acidity and surface area after potassium doping. We discuss the effect of potassium on the relative SCR activity of VSZ_AH and VSZ_ED, leading to a higher activity of the latter, in more detail later.

Comparing the impact of K-doping on the SCR activities of the sulfate- or tungsta-promoted catalysts, it is evident from the remaining SCR activity versus temperature plot in Fig. 8 (bottom) that the sulfated catalysts (especially the ED-prepared sample) had enhanced resistance to potassium. The resistance to alkali doping and the vanadium surface coverage presented in Table 1 suggest that low vanadium coverage, high surface area, and high surface acidity are critical parameters for increased resistance to alkali. KVSZ_ED, with a surface coverage of 2.1 VO_x/nm^2, displayed the greatest remaining activity (Fig. 8, bottom) whereas the severely deactivated KVWZ_AH sample had a surface coverage of 3.5 VO_x/nm^2—almost half a monolayer. For all of the promoted catalysts, the resistance toward potassium poisoning seemed to follow the order VSZ_ED (2.0 VO_x/nm^2) > VSZ_AH (2.8 VO_x/nm^2) > VWT_ref (2.9 VO_x/nm^2) > VWZ_AH (3.4 VO_x/nm^2).

Higher alkali resistance toward potassium of sulfate-promoted catalysts also correlated with the relative strength of the V=O bond of the surface vanadates, detected via in situ Raman spectroscopy. Alkali doping of V_2O_5/ZrO_2 has been reported to result in severe deactivation [14], whereas the corresponding sulfate-promoted catalyst shows considerably better alkali resistance. As discussed above, the V=O stretching frequency is red-shifted from 1029 to 988 cm^{-1} when V_2O_5/ZrO_2 is doped with potassium, whereas the V=O band in the corresponding sulfated catalyst is red-shifted to only 1006 cm^{-1}. The protecting effect of sulfation on the V=O redox site is thus obvious.

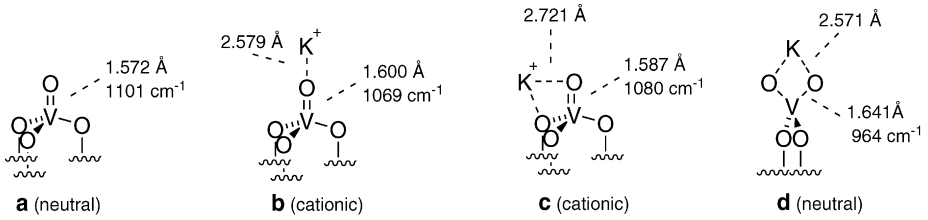

Fig. 9. The three cationic and one neutral monomeric vanadium complexes included in the computational investigation.

3.6. Computational studies

To investigate the possible structural changes responsible for the differences observed in the in situ Raman spectra (Fig. 5) on doping with potassium, we performed a modeling study using density functional theory (DFT) as described in Section 2.8. The SCR reaction has been subject of several theoretical studies [50–53], and a recent quantum mechanical study of the entire SCR reaction on a $V_2O_9H_8$ cluster suggested that the active catalyst consists of a two neighboring vanadium oxo sites [54]. The Brønsted acidic V^{4+} site protonates the incoming NH_3 molecule to form NH_4^+, which is then susceptible to an attack by an NO molecule to form an unstable NH_3NHO adduct, which subsequently decomposes into nitrogen and water. Here we focus on the molecular basis for the detrimental effect observed in the presence of potassium cations ("poisoning"). The main observable change in the in situ Raman spectra on introduction of potassium on the vanadium-based catalyst is the red-shifting of the V=O stretching frequency by approximately 40 cm^{-1}, and the primary objective of our computational study was to gain insight into this phenomenon. The structural effect of alkali metals in general (Li, Na, K, and Rb) have previously been studied by Witko et al. [55] using a relatively large $V_{10}O_{31}H_{12}$ cluster, but in the current study we attempted to also elucidate the changes in the vibrational spectrum.

The structures were all assumed to be singlets (closed-shell species), and only fully oxidized vanadium species were considered (V^{5+}). In a related study by van Dam et al. [56], a series of model systems of increasing size were investigated using similar methods, and it was found that the structure of the vanadium oxide unit did not depend significantly on the size of the computational model system. Thus, in the present work we limited ourselves to relatively simple model systems in which the carrier surface is not explicitly included.

Initially, we considered the isolated V=O moiety with three hydroxyl moieties. To emulate the fixation to the bulk ZrO_2 surface, the capping hydrogen atoms were oriented in the opposite direction of the V=O bond and given a mass of 1000 amu [57]. With this model system, the equilibrium structure has a V=O bond length of 1.572 Å with a stretching frequency of 1101 cm^{-1}, and three identical V–O bonds with a length of 1.780 Å (Fig. 9a). Compared with the experimental in situ Raman spectra, the calculated vibrational frequency appears at a slightly higher wavenumber, which could be related to the fact that under experimental conditions, a fraction of the vanadia atoms are in a lower oxidation state. But because we are concerned mainly with the change in stretching frequency on poisoning with potassium, the exact location of the band is not crucial.

To probe the effect of potassium poisoning on the structural features of the V=O moiety, a single potassium ion was included, and two different positions were investigated for the monomer: coordination to potassium with the double-bonded oxygen (Fig. 9b) and coordination between two oxygen atoms (Fig. 9c). Finally, a deprotonated model structure in which the negative charge became delocalized between two equivalent oxygen atoms was considered (Fig. 9d).

Coordination of the potassium cation to the double-bonded oxygen atom resulted in the expected elongation of the V=O bond to 1.600 Å while simultaneously contracting the three V–O single bonds by 0.20–0.25 Å (Fig. 9b). The increased bond length for the V=O bond was accompanied by a red shift of the V=O stretching of 32 cm^{-1}, in good agreement with the value derived from the experimental spectrum, where a red shift from 1029 cm^{-1} (1.581 Å) to 988 cm^{-1} (1.603 Å) was observed when V_2O_5/ZrO_2 was doped with potassium (Fig. 5). When the potassium ion was instead coordinated by two oxygen atoms as in model c (Fig. 9), then the calculated change in the V=O stretching frequency was decreased by 21 cm^{-1}, and the concomitant increase in bond length was significantly smaller (0.015 Å vs 0.028 Å for b). The energy for the structural isomers b and c can be compared directly; with the methods used here, we found them to be virtually equienergetic (with model c favored by only 2 kJ/mol in Gibbs free energy).

On deprotonation, there is a strong tendency to form a structure in which the potassium atom is coordinated between two equivalent oxygen atoms, leaving only two anchoring points to the carrier (Fig. 9d). The two V–O bonds now have identical lengths of 1.641 Å, considerably longer than for the other K^+-doped structures, indicating additional weakening of the former V=O bond, which is also observable in the large shift in frequency of 137 cm^{-1}. A shift of this magnitude is more dramatic than that observed in the experimental spectra, indicating that structures of this type are not dominating under experimental conditions. We calculated atom-centered point charges on V, O, and K using both Mulliken and ESP schemes; these are given in Table 4. On introduction of potassium (cf. Figs. 9a and 9b), the polarization of the V=O bond was increased, resulting in an overall weakening of the bond ($V_{\delta+}$–$O_{\delta-}$). There was little difference between the two coordination modes for the cationic vanadium complexes (Figs. 9b and 9c); however, the interaction between potassium and the oxygen atoms was stronger for the deprotonated complex (Fig. 9d), leading to the largest decrease in the positive charge on potassium.

Table 4
Calculated Mulliken and ESP atomic charges for V, O, and K in monomeric vanadium complexes listed in Figs. 9a–9d

Model system	Mulliken charge (V)	ESP charge (V)	Mulliken charge (=O)	ESP charge (=O)	Mulliken charge (K^+)	ESP charge (K^+)
9a	+1.22	+1.20	−0.36	−0.35	–	–
9b	+1.33	+1.23	−0.70	−0.64	+0.94	+0.98
9c	+1.33	+1.25	−0.69	−0.64	+0.92	+0.98
9d	+1.17	+1.28	−0.65	−0.72	+0.87	+0.94

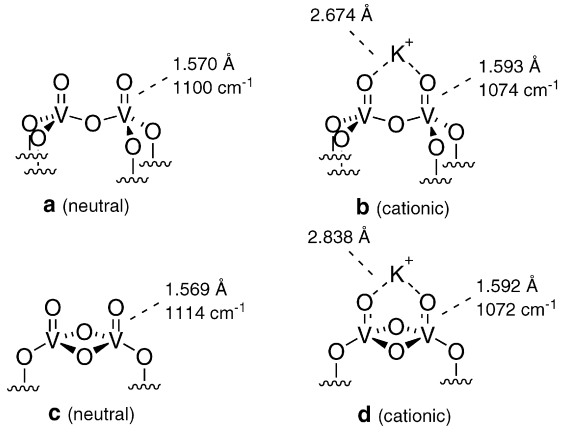

Fig. 10. The two forms of dimeric vanadia-oxo moieties used to examine the influence of potassium poisoning. Above: The monooxo-bridged vanadia dimer. Below: The dioxo-bridged vanadia dimer.

It is well known that the vanadium oxo moieties can condense to form polymers under the reaction conditions with resulting loss of catalytic activity. To investigate this, we chose the monooxo-bridged (a, Fig. 10) and dioxo-bridged dimers (c, Fig. 10) as models. For both undoped dimers, the equilibrium V=O distance was approximately 1.570 Å, which in both cases was elongated by 0.023 Å on complexation with a K^+ ion (b and d, Fig. 10). These calculated increases in bond lengths correlate well with that derived from the in situ Raman spectra (0.02 Å; spectra c and d in Fig. 5).

The increased strain in the dioxo dimer in Fig. 10c resulted in a slightly higher V=O stretching frequency (1114 cm^{-1} vs 1100 cm^{-1} for a in Fig. 10), and in both cases a red shift of the V=O stretching frequency on complexation with the potassium ion to ∼1070 cm^{-1} was observed (b: 1074 cm^{-1}; d: 1072 cm^{-1}). Note that the calculated red shift for the monooxo dimer of 36 cm^{-1} is in excellent agreement with the experimental value, whereas the calculated shift for the dioxo dimer appears to be too high. The calculated Mulliken and ESP charges for the dimeric vanadium complexes are shown in Table 5. The coordination of potassium also resulted in polarization of the V=O bond, although to a lesser extent than that for the monomers, as demonstrated by the partial negative charge on oxygen. The magnitude of this polarization was slightly larger for the monooxo-bridged dimer than for the dioxo-bridged dimer (cf. Figs. 10b and 10d), possibly due to the larger distance between the oxygen atoms and potassium in the more strained dioxo-bridged dimer.

Table 5
Calculated Mulliken and ESP atomic charges for V, O, and K in dimeric vanadium complexes listed in Figs. 10a–10d

Model system	Mulliken charge (V)	ESP charge (V)	Mulliken charge (=O)	ESP charge (=O)	Mulliken charge (K^+)	ESP charge (K^+)
10a	+1.28	+1.32	−0.35	−0.38	–	–
10b	+1.38	+1.38	−0.51	−0.54	+0.90	+0.97
10c	+1.32	+1.34	−0.36	−0.42	–	–
10d	+1.40	+1.38	−0.47	−0.53	+0.91	+0.96

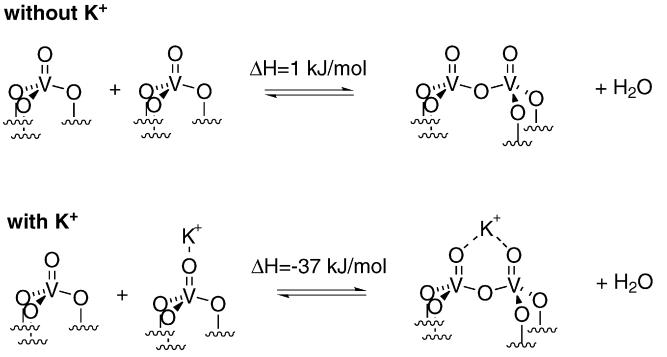

Fig. 11. Effect of potassium on the equilibrium between monomeric and dimeric vanadia complexes.

With the energies for both monomeric and dimeric vanadium complexes available, it is possible to examine the condensation (dimerization) equilibrium as illustrated in Fig. 11. In the absence of potassium ions, the enthalpy of formation of the dimer with a mono-oxygen bridge was almost thermoneutral ($\Delta H = 1$ kJ/mol); however, the liberation of water at high temperatures still may have allowed such formation to a certain extent. In the presence of potassium, formation of the dimer was clearly favored in enthalpy ($\Delta H = -37$ kJ/mol), which readily explains the increase of the V–O–V bands at around 800 cm^{-1} observed experimentally in Figs. 5 and 6 with K-doping of V_2O_5/ZrO_2. This also correlates well with the findings of Chen and Yang [9], who measured the SCR activity of V_2O_5/TiO_2 versus the K/V molar ratio and found that the catalyst deactivated almost completely at K/V ≈ 0.5, because one potassium unit was coordinated to two VO_x units. For the dioxo-bridged dimer in Fig. 9, the dimerization was very unfavorable ($\Delta H = 135$ kJ/mol), and there was only a negligible effect of potassium on the enthalpy of dimerization. Presumably, this was due to the additional strain in the dioxo-bridged species, which forced the two coordinating oxygen atoms further away from the potassium by about 0.2 Å, thus preventing efficient coordination.

The position of the monomeric–dimeric equilibrium of the vanadate species in the presence of potassium can provide a possible explanation for the observed potassium-induced deactivation of catalysts with relatively high surface coverage. Comparing the vanadium surface coverage and deactivation on potassium doping of the two iso-acidic sulfated catalysts, VSZ_AH and VSZ_ED (Table 1) illustrates an interesting point. The main difference between the samples is the surface area and, consequently, the acid site concentration and vana-

dium coverage. From the computational studies, we found that dimerization (resulting in loss of active sites) of the monomeric vanadate units was favored in enthalpy when potassium was present. Considering the impact of surface coverage, the dimerization of vanadate monomers should be preferred for the catalyst with the highest coverage [i.e., VSZ_AH (2.8 VO_x/nm^2) over VSZ_ED (2.0 VO_x/nm^2)], which correlates well with the observed catalytic measurements. The relatively high loss of acidity of the VSZ_AH catalyst by K-doping is thus understandable, because dimerization occurs by destruction of two V–OH Brønsted sites (liberating a H_2O molecule).

4. Conclusion

The characterization of vanadia-based SCR catalysts, promoted by sulfate or tungsten oxide supported on zirconia prepared from precipitated hydrous zirconia, showed that the catalyst structure and SCR activity were affected by the synthesis route, especially by the choice of the $Zr(OH)_4$-precipitant. Using ethylene diamine in the precipitation of hydrous zirconia resulted in overall higher surface areas and a higher fraction of crystalline tetragonal ZrO_2 compared with using ammonium hydroxide as the precipitant. Conversely, TGA–MS data showed that sulfate-impregnated samples obtained after precipitation with ammonium hydroxide formed more stable sulfate species, decomposing to SO_2 at around 700–1000 °C, whereas the corresponding ethylene diamine-precipitated samples started liberating SO_2 already at 500 °C.

Doping the vanadia-based SCR catalysts with potassium to a K/V molar ratio of 0.4 was proved by in situ Raman spectroscopy to affect the stretching frequency (i.e., strength and length) of the V=O bond in surface vanadates. This indicates that potassium altered the active vanadium surface species in the SCR reaction, lengthening the V=O bond. Catalyst promotion by sulfate resulted in a lower degree of V=O bond lengthening on potassium doping, which can account for the higher resistance to alkali doping of sulfate-promoted vanadia-based SCR catalysts. This suggests that the active VO_x units are less affected by potassium if the catalyst is sulfated (i.e., have strong surface acid sites). Here the acidic support functioned as a host for the potassium, which was bound preferentially to the strongest acid sites, the sulfated zirconia, over the catalytic active vanadate sites.

The effect of potassium on the V=O bond could not be studied in the in situ Raman spectra of the tungstate-promoted catalysts, where the Raman bands due to formation of crystalline WO_3 obscured the V=O stretching frequency range. The degree of deactivation due to potassium doping seems to be proportional to the vanadium coverage for the samples in focus. The highest alkali resistance decreased in the order VSZ_ED (2.0 VO_x/nm^2) > VSZ_AH (2.8 VO_x/nm^2) > VWT_ref (2.9 VO_x/nm^2) > VWZ_AH (3.4 VO_x/nm^2). This correlates well with the results from the computational studies, which predicted that the dimerization of vanadate monomers would be favored in enthalpy if potassium were present. In other words; low surface vanadium coverage reduces the possibility of potassium-induced dimerization with resulting loss of active sites.

In the computational investigation, we analyzed the structural effects of potassium poisoning in detail and found good qualitative correlation with the in situ Raman measurements. This supports the proposition that a coordination interaction between K^+ and two neighboring V=O is responsible for the observable decrease in V=O stretching frequency, and also provides a rationale for the observed higher proportion of dimers and higher polymers in the presence of potassium cations. The scenario proposed here of K^+ joining two VO_x units under the liberation of H_2O agrees well with the experimental observations of almost complete deactivation of the V_2O_5/TiO_2 SCR catalyst by potassium salts at a K/V molar ratio of ∼0.5.

These results provide new insight into the previously reported improved resistance of sulfate- and tungstate-promoted SCR catalysts to poisoning with potassium compared with traditional V_2O_5/TiO_2 catalyst. In the case of acidic supports, the potassium preferentially interacts with promoter surface species (sulfate or tungstate), leaving a part of the vanadium-based sites, which are responsible for the catalytic activity, largely unaffected.

We believe that the detailed information reported herein may prove valuable in the development of new catalysts with improved resistance toward alkali poisoning.

Acknowledgments

The Center for Sustainable and Green Chemistry is sponsored by the Danish National Research Foundation. This work was supported by Energinet.dk (project PSO-FU5201). The authors thank MAX-lab, Sweden, for facilitating the high-temperature XRD measurements.

Supporting information

XYZ coordinates, SCF energies and additional thermodynamic data are available for all structures discussed in the manuscript.

Please visit DOI: 10.1016/j.jcat.2007.07.016.

References

[1] G. Busca, L. Lietti, G. Ramis, F. Berti, Appl. Catal. B 18 (1998) 1.
[2] V.I. Pârvulescu, P. Grange, B. Delmon, Catal. Today 46 (1998) 233.
[3] N.-Y. Topsøe, H. Topsøe, J.A. Dumesic, J. Catal. 151 (1995) 226.
[4] N.-Y. Topsøe, J.A. Dumesic, H. Topsøe, J. Catal. 151 (1995) 241; N.-Y. Topsøe, Science 265 (1994) 1217.
[5] I.E. Wachs, G. Deo, B.M. Weckhuysen, A. Andreini, M.A. Vuurman, M. de Boer, M.D. Amiridis, J. Catal. 161 (1996) 211.
[6] J.A. Dumesic, N. Topsøe, H. Topsøe, Y. Chen, T. Slabiak, J. Catal. 163 (1996) 409.
[7] M. Anstrom, J.A. Dumesic, N.-Y. Topsøe, Catal. Lett. 78 (2002) 281.
[8] Y. Zheng, A.D. Jensen, J.E. Johnsson, Appl. Catal. B 60 (2005) 253.
[9] J.P. Chen, R.T. Yang, J. Catal. 125 (1990) 411.
[10] H. Kamata, K. Takahashi, C.U.I. Odenbrand, J. Mol. Catal. A 139 (1999) 189.
[11] I.E. Wachs, B.M. Weckhuysen, Appl. Catal. A 137 (1997) 67.
[12] D. Bulushev, F. Rainone, L. Kiwi-Minsker, A. Renken, Langmuir 17 (2001) 5276.

[13] R. Khodayari, C.U.I. Odenbrand, Appl. Catal. B 30 (2001) 87.
[14] A.L. Kustov, M.Y. Kustova, R. Fehrmann, P. Simonsen, Appl. Catal. B 58 (2005) 97;
A.L. Kustov, S.B. Rasmussen, P. Simonsen, R. Fehrmann, Appl. Catal. B (2007), doi:10.1016/j.apcatb.2007.05.004.
[15] J. Due-Hansen, A.L. Kustov, S.B. Rasmussen, R. Fehrmann, C.H. Christensen, Appl. Catal. B 66 (2006) 160.
[16] K. Bourikas, Ch. Fountzoula, Ch. Kordulis, Appl. Catal. B 52 (2004) 145.
[17] I. Giakoumelou, Ch. Fountzoula, Ch. Kordulis, S. Boghosian, J. Catal. 239 (2006) 1.
[18] J.G. Santiesteban, J.C. Vartuli, S. Han, R.D. Bastian, C.D. Chang, J. Catal. 168 (1997) 431.
[19] L. D'Souza, A. Suchopar, K. Zhu, D. Balyozova, M. Devadas, R.M. Richards, Microporous Mesoporous Mater. 88 (2006) 22.
[20] J.R. Sohn, M.Y. Park, Langmuir 14 (1998) 6140.
[21] M.G. Cutrufello, U. Diebold, R.D. Gonzalez, Catal. Lett. 101 (2005) 5.
[22] A. Christodoulakis, S. Boghosian, J. Catal. 215 (2003) 139.
[23] C. Lee, W. Yang, R.G. Parr, Phys. Rev. B 37 (1988) 785.
[24] A.D. Becke, J. Chem. Phys. 98 (1993) 5648.
[25] A.D. Becke, J. Chem. Phys. 98 (1993) 1372.
[26] Jaguar, version 6.5, release 106, Schrodinger, LLC, New York, NY, 2005.
[27] P.J. Hay, R.W. Wadt, J. Chem. Phys. 82 (1985) 299.
[28] R. Ditchfield, W.J. Hehre, J.A. Pople, J. Chem. Phys. 54 (1971) 724.
[29] R.S. Mulliken, J. Chem. Phys. 23 (1955) 1833.
[30] L.E. Chirlian, M.M. Francl, J. Comput. Chem. 8 (1987) 894.
[31] R.J. Woods, M. Khalil, W. Pell, S.H. Moffat, V.H. Smith Jr., J. Comput. Chem. 11 (1990) 297.
[32] C.M. Breneman, K.B. Wiberg, J. Comput. Chem. 11 (1990) 361.
[33] A.P. Scott, L. Radom, J. Phys. Chem. 100 (1996) 16502.
[34] H. Tian, E.I. Ross, I.E. Wachs, J. Phys. Chem. B 110 (2006) 9593.
[35] X. Yang, F.C. Jentoft, R.E. Jentoft, F. Girgsdies, T. Ressler, Catal. Lett. 81 (2002) 25.
[36] N. Yi, Y. Cao, W. Feng, W. Dai, K. Fan, Catal. Lett. 99 (2005) 73.
[37] K. Arata, M. Hino, Mater. Chem. Phys. 26 (1990) 213.
[38] J.P. Chen, R.T. Yang, J. Catal. 139 (1993) 277.
[39] J.P. Dunn, J.-M. Jehng, D.S. Kim, L.E. Briand, H.G. Stenger, I.E. Wachs, J. Phys. Chem. B 102 (1998) 6212.
[40] A. Christodoulakis, M. Machli, A.A. Lemonidou, S. Boghosian, J. Catal. 222 (2004) 293.
[41] G. Ramis, G. Busca, F. Bregani, Catal. Lett. 18 (1993) 299.
[42] D.S. Kim, M. Ostromecki, I.E. Wachs, J. Mol. Catal. A 106 (1996) 93.
[43] F. Figueras, J. Palomeque, S. Loridant, C. Feche, N. Essayem, G. Gelbard, J. Catal. 226 (2004) 25.
[44] M. Scheithauer, R.K. Grasselli, H. Knözinger, Langmuir 14 (1998) 3019.
[45] M. Boulova, G. Lucazeau, J. Solid State Chem. 167 (2002) 425.
[46] M.A. Vuurman, I.E. Wachs, A.M. Hirt, J. Phys. Chem. 95 (1991) 9928.
[47] I.E. Wachs, Catal. Today 100 (2005) 79.
[48] F.D. Hardcastle, I.E. Wachs, J. Phys. Chem. 95 (1991) 5031.
[49] A. Christodoulakis, E. Heracleous, A.A. Lemonidou, S. Boghosian, J. Catal. 242 (2006) 16.
[50] F. Gilardoni, J. Weber, A. Baiker, J. Phys. Chem. A 101 (1997) 6069.
[51] M. Anstrom, N.-Y. Topsøe, J.A. Dumesic, J. Catal. 213 (2003) 115.
[52] K. Jug, T. Homann, T. Bredow, J. Phys. Chem. A 108 (2004) 2966.
[53] A. Vittadini, M. Casarin, A. Selloni, J. Phys. Chem. B 109 (2005) 1652.
[54] S. Soyer, A. Uzun, S. Senkan, I. Onal, Catal. Today 118 (2006) 268.
[55] M. Witko, R. Grybos, R. Tokarz-Sobieraj, Top. Catal. 38 (2006) 105.
[56] H.J.J. van Dam, M.F. Guest, P. Sherwood, J.M.H. Thomas, J.H. van Lenthe, J.N.J. van Lingen, C.L. Bailey, I.J. Bush, J. Mol. Struct. (THEOCHEM) 771 (2006) 33.
[57] V.I. Avdeev, G.M. Zhidomirov, J. Struct. Chem. 46 (2005) 577.